Electronic Supplementary Material (ESI) for Soft Matter.

Supplementary Information for "Morphology, repulsion, and ordering of red blood cells in viscoelastic flows under confinement"

Steffen M. Recktenwald[a,b,*], Yazdan Rashidi[a], Ian Graham[c], Paulo E. Arratia[c], Francesco Del Giudice[d], and Christian Wagner[a,e]

[a]Dynamics of Fluids, Department of Experimental Physics, Saarland University, 66123 Saarbrücken, Germany
[b]Micro/Bio/Nanofluidics Unit, Okinawa Institute of Science and Technology Graduate University, 1919-1 Tancha, Onna-son, Okinawa 904-0495, Japan
[c]Department of Mechanical Engineering and Applied Mechanics, University of Pennsylvania, Philadelphia, PA 19104, USA
[d]Complex Fluid Research Group, Department of Chemical Engineering, Faculty of Science and Engineering, Swansea University, Swansea SA1 8EN, United Kingdom
[e]Physics and Materials Science Research Unit, University of Luxembourg, L-1511 Luxembourg, Luxembourg
[*]steffen.recktenwald@uni-saarland.de

Materials

Besides the HA and PEO solutions, we investigated the flow of RBCs in fluids with a near-constant viscosity. Therefore, we used a density gradient medium based on a 60 % iodixanol solution in water (Optiprep, Sigma-Aldrich, Taufkirchen, Germany), an isotonic polyvinylpyrrolidone (PVP, RR Mechatronics, Zwaag, The Netherlands), and an infusion solution that is clinically used as volume replacement fluid (VRF) after blood loss (Gelafundin ISO 40 mg/mL, B. Braun Melsungen AG, Melsungen, Germany). The rheological data is presented in Fig. S3 summarized in Table 1.

Methods

We determined the extensional flow behavior of the used fluids in uniaxial extension. For this, we studied the thinning and breakup of stretched fluid filaments with a customized capillary extensional breakup rheometer (CaBER) device. The fluid sample was placed between two circular steel plates with a diameter of 4 mm. The lower plate was fixed and the upper plate was drawn apart with a linear motor (P01-23×80, Linmot, Spreitenbach, Switzerland). A high-speed camera (X-Stream XS-5, IDT, Tallahassee, FL) with LED illumination, a tube lens, and a 2× air objective (Plan, Nikon, Melville, NY) with a numerical aperture $NA = 0.06$ were used to measure the minimal neck diameter $D(t)$ of the fluid filament as a function of time.

Flow behavior in uniaxial extension

Figure S4 shows the evolution of the minimum diameter of the stretched fluid filament for the used fluids. The time $(t - t_b)$ is normalized by the breakage time t_b of the fluid filaments when the capillary bridge ruptures. The inset images in Fig. S4 show the typical filament shape of the corresponding sample close to the last stage of the thinning process. The axial filament profiles of the control, iodixanol, and VRF are axially nonuniform throughout the whole thinning process, indicative of the breakup behavior of a Newtonian fluid in uniaxial extension. For the other samples, the axial profile evolves into an axially uniform cylindrical filament that connects the two roughly hemispherical fluid reservoirs near the endplates. During this stage, the filament diameter decreases exponentially with time, as indicated by the red lines in Fig. S4. This observation implies the presence of elasticity under extensional flow due to the suspended polymers in the HA and PEO solutions as well as for the PVP solution.

Supplementary Tables and Figures

Table 1. Overview of the used fluid properties of the constant viscosity fluids.

sample	m_{osm} (mOsm/kg)	η_0 (mPa s)
iodixanol	345.5 ± 9.4	18.7 ± 0.3
PVP	295.3 ± 2.1	42.9 ± 0.7
VRF	280.1 ± 2.2	2.4 ± 0.1

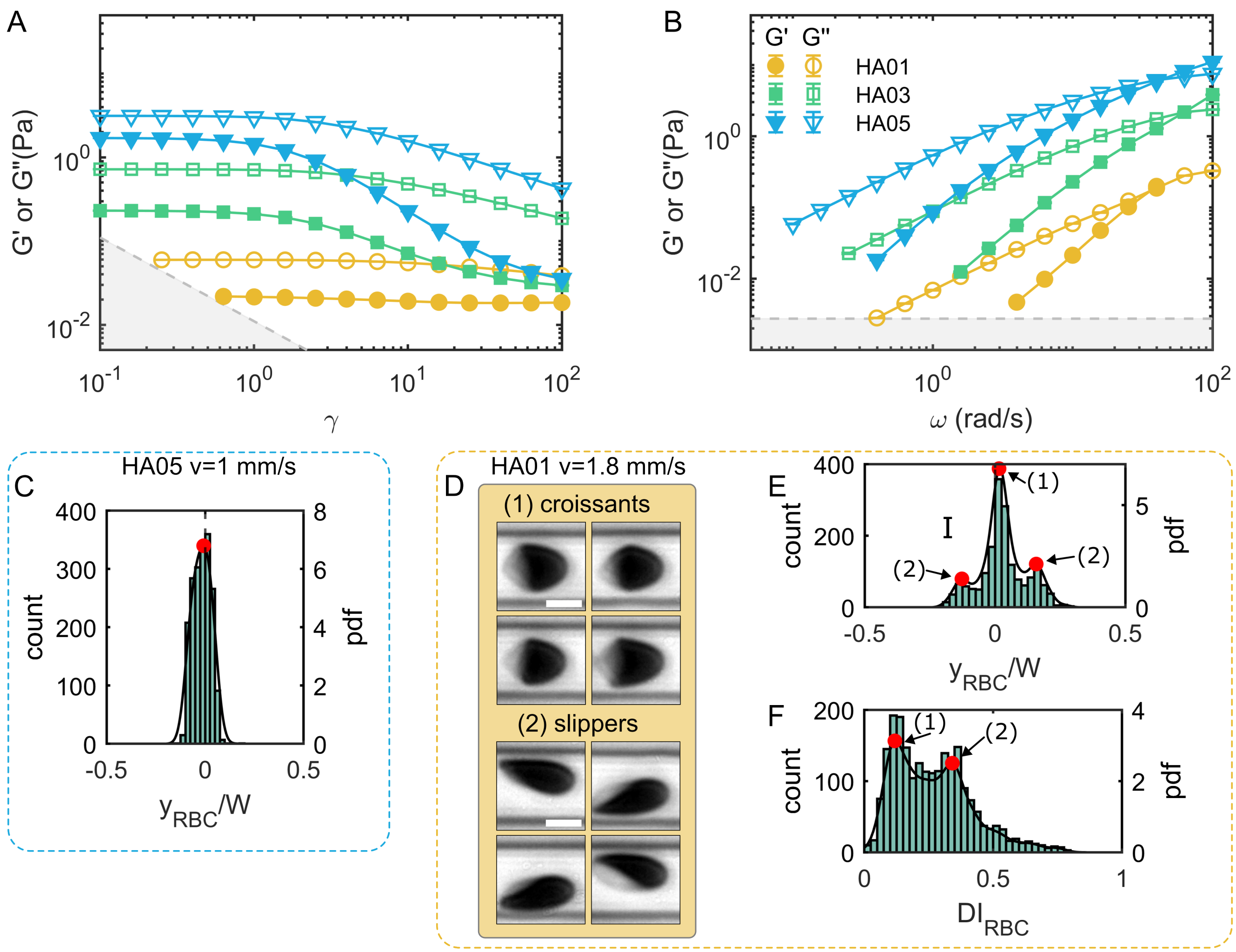

Figure S1. (A) Storage (G') and loss (G'') moduli of the HA solutions as a function of the deformation at a constant angular frequency of 10 rad/s. (B) Storage and loss moduli as a function of the angular frequency at a constant deformation of 0.5. Dashed gray lines and areas the lower torque limit of the device. (C) Representative histogram and probability density distribution (PDF) by kernel density estimation of the normalized y-position across the channel width y_{RBC}/W for the HA05 solution at an RBC velocity of $v = 1$ mm/s. (D-F) Representative RBC flow in the HA01 solution at an RBC velocity of $v = 1.8$ mm/s. (D) Representative snapshots of (1) croissant and (2) slipper-shaped RBCs in HA01. (Scale bars, 5 µm). Histograms and PDFs of (E) the normalized y-position across the channel width y_{RBC}/W and (F) the deformability index DI_{RBC}. Numbers (1) and (2) in panels (E–F) indicate the peaks that emerge due to the presence of the two shape types shown in (D).

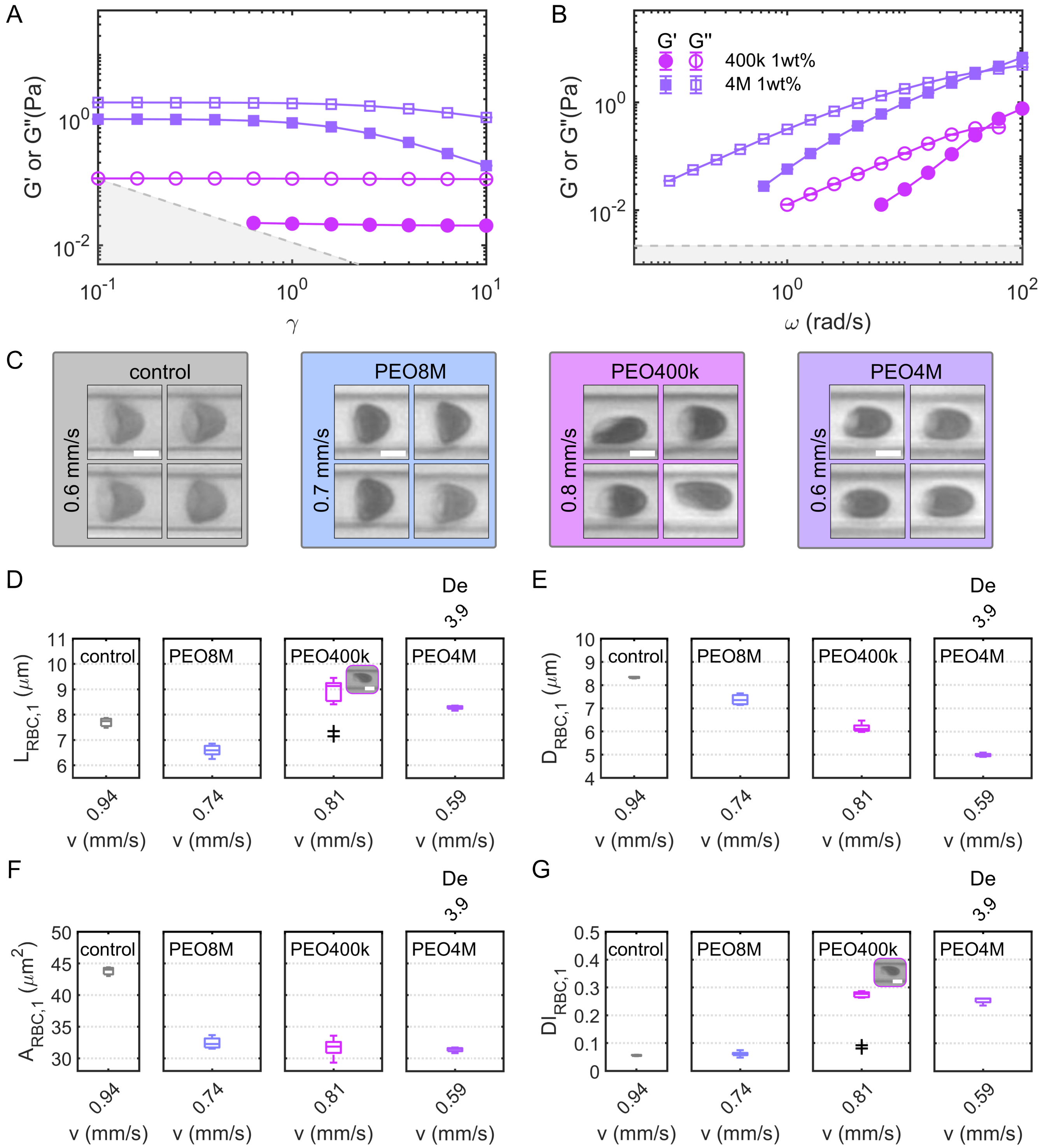

Figure S2. (A) Storage (G' and loss (G'') moduli of the PEO solutions as a function of the deformation at a constant angular frequency of 10 rad/s. (B) Storage and loss moduli as a function of the angular frequency at a constant deformation of 0.5. Dashed gray lines and areas the lower torque limit of the device. (C) Representative images of RBC shapes in the PEO solutions. (Scale bars, 5 µm). (D–G) Boxplots of the single-cell length, diameter, projection area, and deformability index, respectively. The inset images for PEO 400k in (D–G) show representative slipper-shaped RBCs that emerge in this solution and lead to an apparent increase in the RBC length and deformability index. (Scale bars, 5µm). The bottom and top of each box are the 25th and 75th percentiles of the sample, respectively. The line in the middle of each box is the sample median. Whiskers go from the end of the interquartile range to the furthest observation. Data beyond the whisker length are marked as outliers with '+' signs.

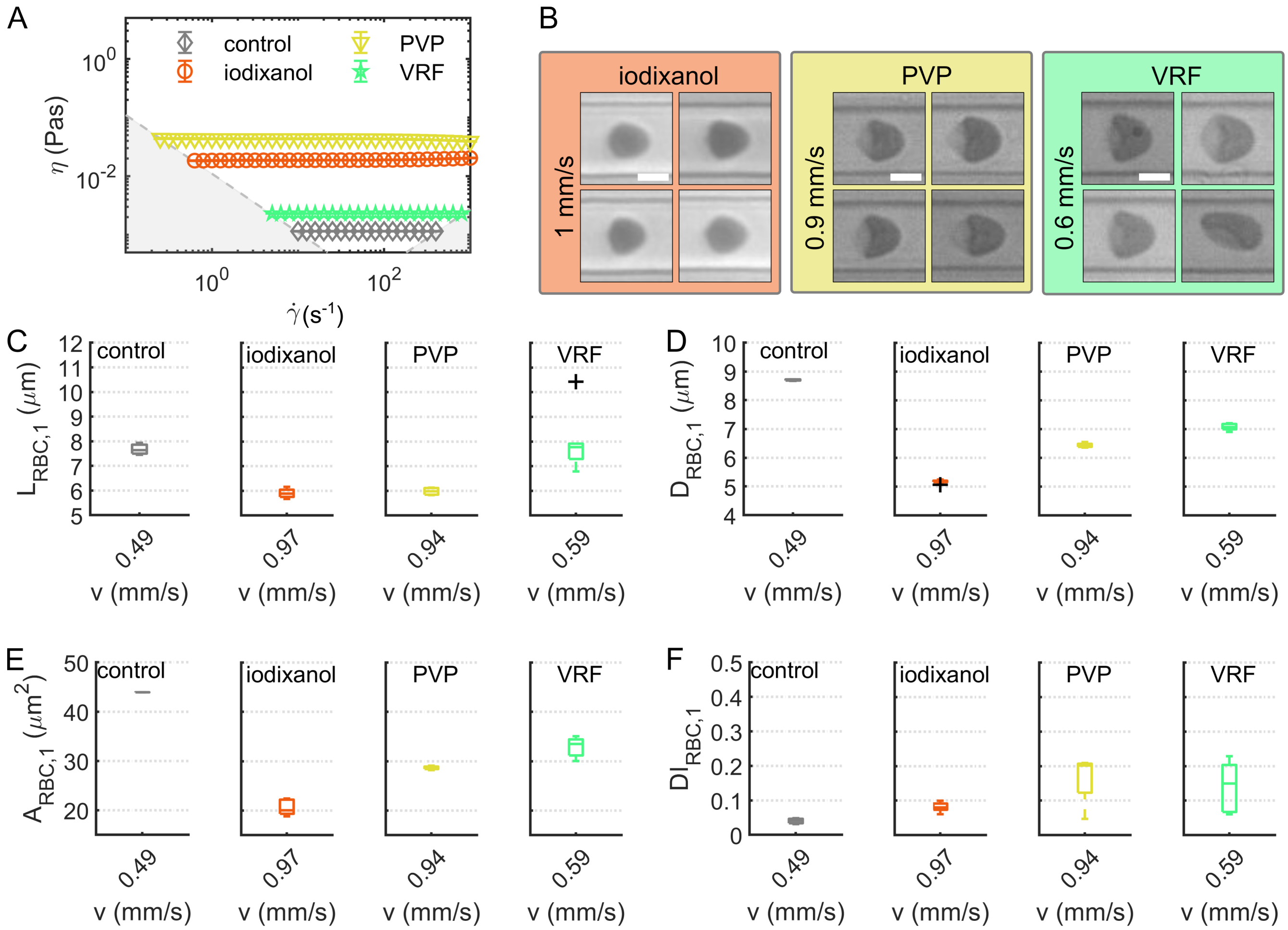

Figure S3. (A) Rheological fluid characterization of the constant viscosity fluids using steady shear measurements. Dashed gray lines and areas the lower torque limit of the device. (B) Representative images of RBC shapes. (Scale bars, 5 µm). (C–F) Shape characteristics of single RBCs during flow. Boxplots of the single-cell length, diameter, projection area, and deformability index, respectively. The bottom and top of each box are the 25th and 75th percentiles of the sample, respectively. The line in the middle of each box is the sample median. Whiskers go from the end of the interquartile range to the furthest observation. Data beyond the whisker length are marked as outliers with '+' signs.

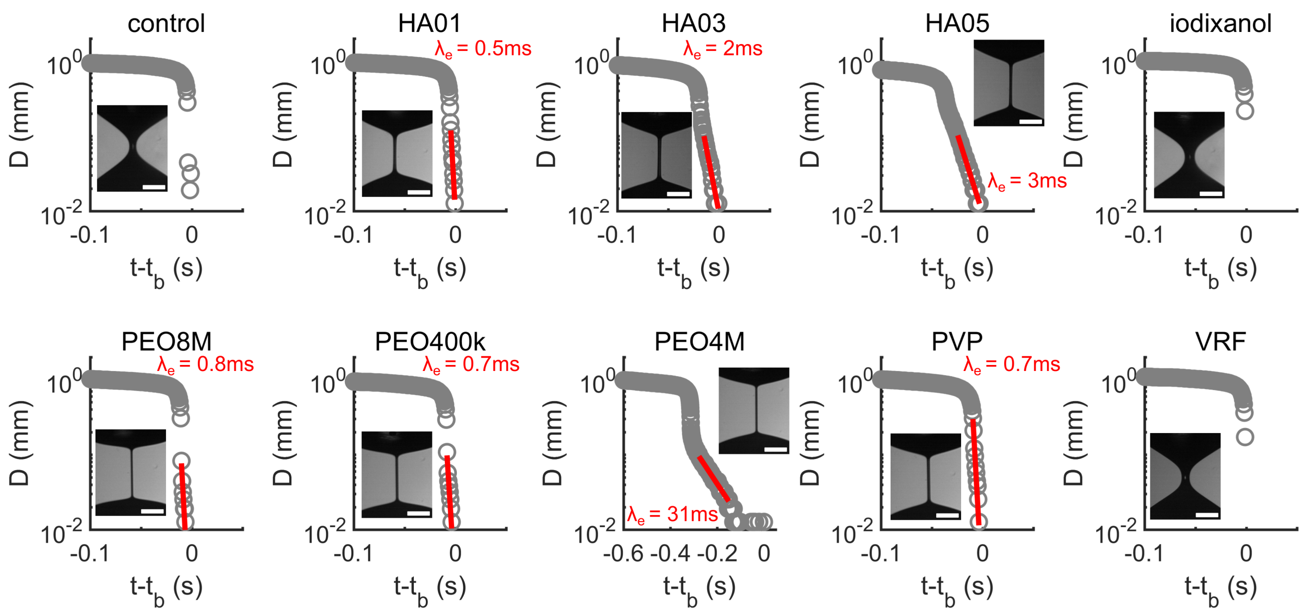

Figure S4. Filament breakup during capillary thinning of the used fluids. Data is shown as minimal filament diameter D as a function of time t until the filament breakup at t_b. Red lines show exponential fits to the respective measured data. The extensional relaxation time λ_e is derived from these fits and depicted in the corresponding panel. The inset images show the filaments close at the last stage of the thinning process close to the breakup. (Scale bars, 0.5 mm).

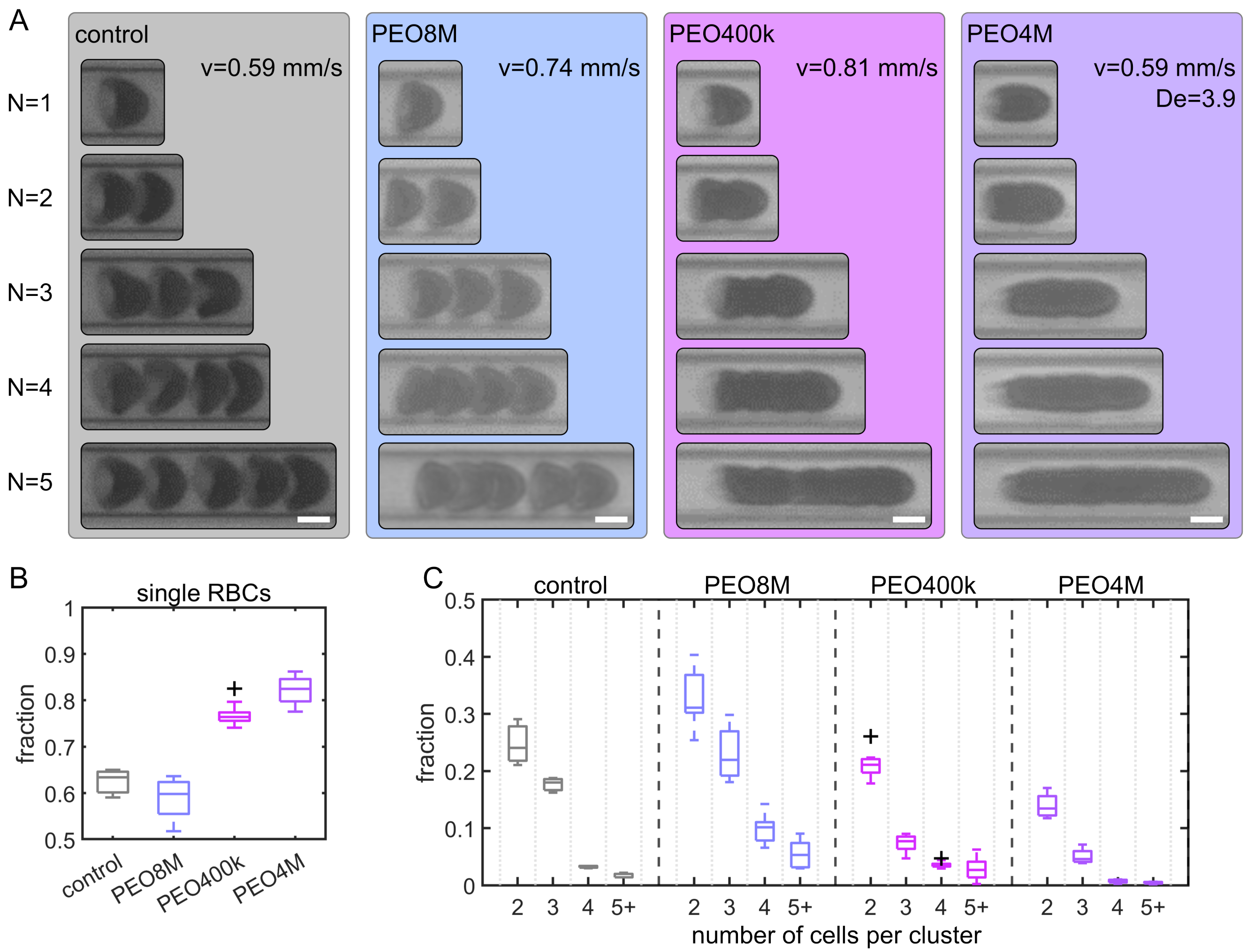

Figure S5. (A) Representative snapshots of clusters containing N=1-5 RBCs (top to bottom) for the different PEO samples. (Scale bars, 5 µm). For the control and PEO8M, the individual RBCs can be discriminated within the clusters. Individual RBCs adhere closely to one another for the PEO solutions and cannot be distinguished within the clusters. (B) Fraction of single RBCs that are spaced further than one RBC length apart and that do not belong to an adhering cluster. (C) Fraction of RBC clusters with different lengths. The x-axes label 5+ denotes clusters with $N = 5$ or more RBCs. The x-axis shows the number of RBCs per cluster. The bottom and top of each box are the 25th and 75th percentiles of the sample, respectively. The line in the middle of each box is the sample median. Whiskers go from the end of the interquartile range to the furthest observation. Data beyond the whisker length are marked as outliers with '+' signs.

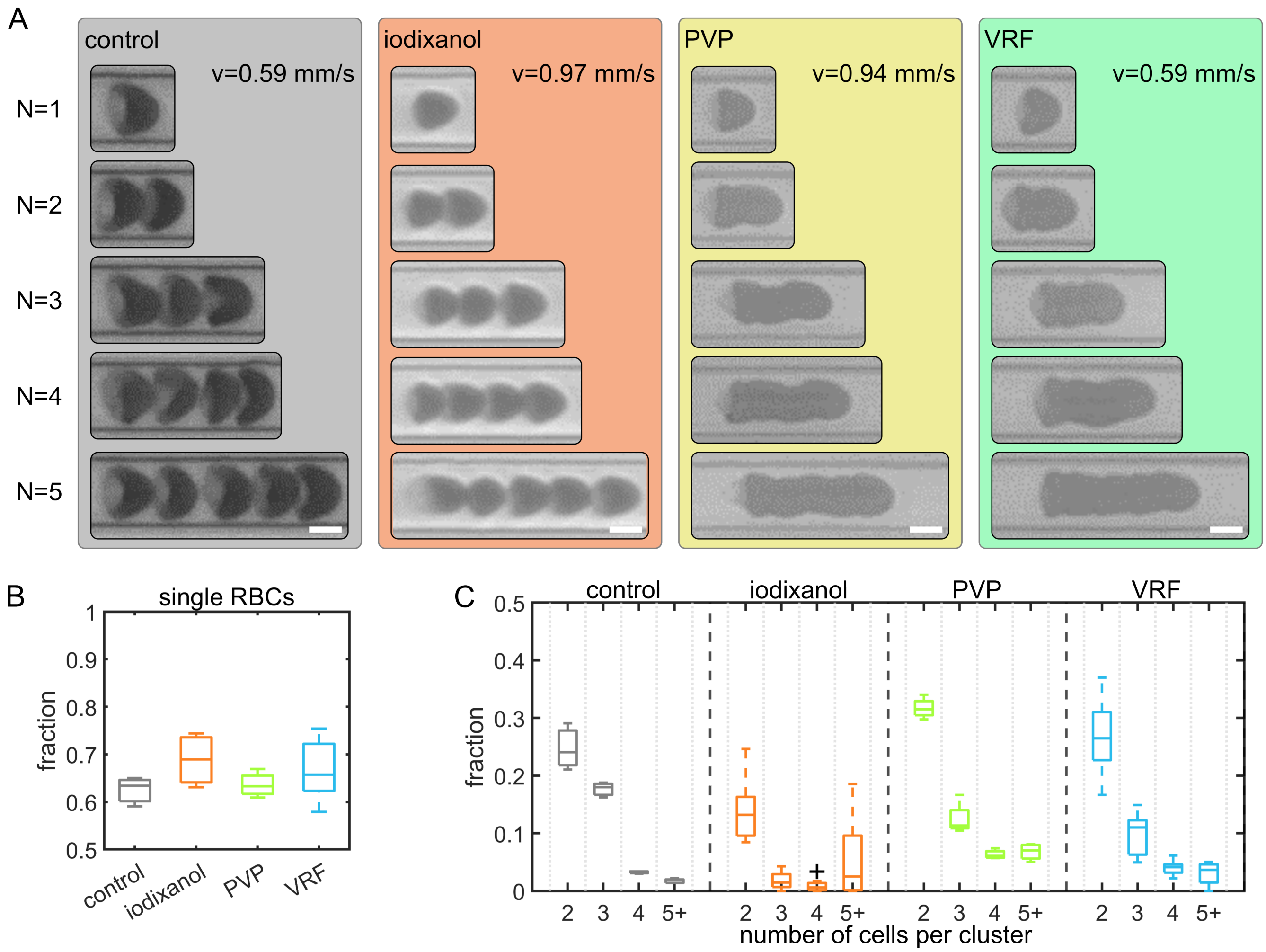

Figure S6. (A) Representative snapshots of clusters containing $N = 1 - -5$ RBCs (top to bottom) for the different constant viscosity fluids. (Scale bars, 5 µm). For the control and iodixanol, the individual RBCs can be discriminated within the clusters. Individual RBCs adhere closely to one another for the other solutions and cannot be discriminated within the clusters. (B) Fraction of single RBCs that are spaced further than one RBC length apart and that do not belong to an adhering cluster. (C) Fraction of RBC clusters with different lengths. The x-axis shows the number of RBCs per cluster. The x-axes label 5+ denotes clusters with $N = 5$ or more RBCs. The bottom and top of each box are the 25th and 75th percentiles of the sample, respectively. The line in the middle of each box is the sample median. Whiskers go from the end of the interquartile range to the furthest observation. Data beyond the whisker length are marked as outliers with '+' signs.

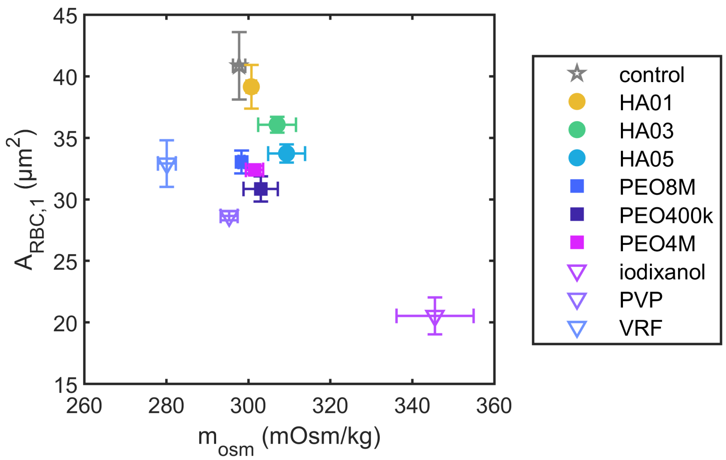

Figure S7. Single-cell projection area $A_{RBC,1}$ as a function of the suspended medium osmolality. Error bars correspond to averaging over all cell velocities for each sample.

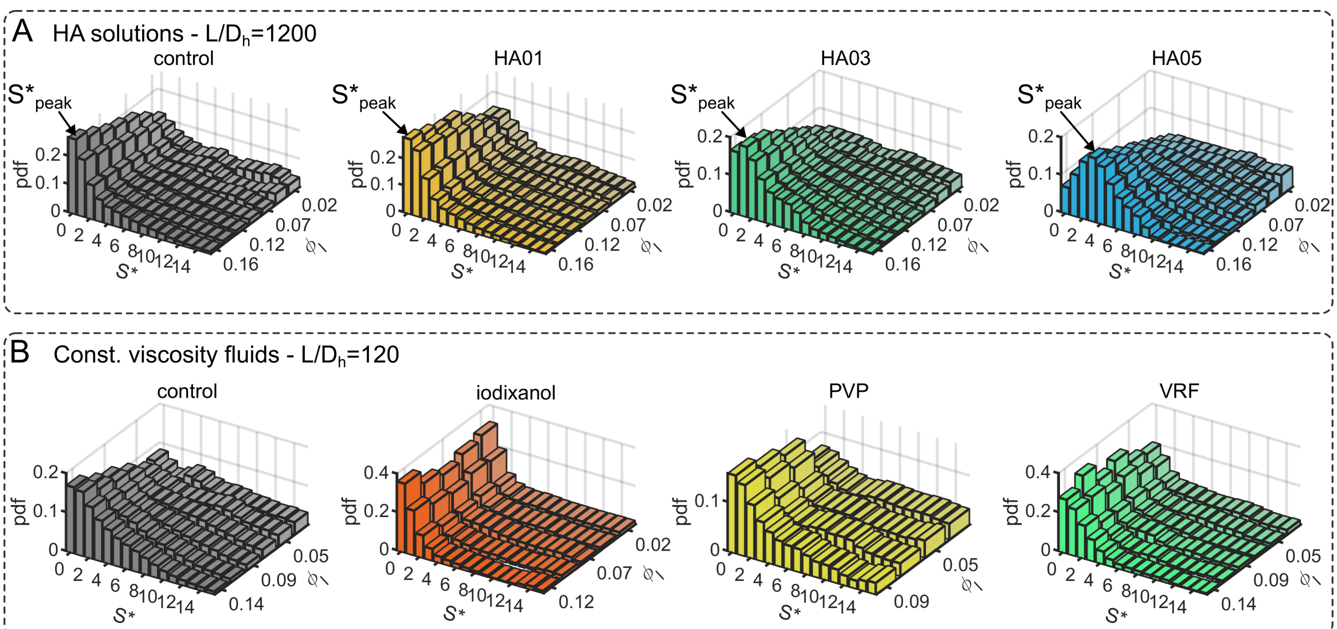

Figure S8. (A) Probability density distributions (pdf) of the normalized distance $S^* = s/L_{RBC,1}$ for the different samples as a function of the local RBC concentration ϕ_l. Data is shown for control ($v = 0.6$ mm/s, $De = 0$), HA01 ($v = 1.8$ mm/s, $De = 0.4$), HA03 ($v = 1.2$ mm/s, $De = 1.9$), and HA05 ($v = 1$ mm/s, $De = 6.3$) at $L/D_h = 1200$. The arrows indicate the peak value of the corresponding pdf at the highest local concentration. (B) PDFs of the normalized distance $S^* = s/L_{RBC,1}$ for the different constant viscosity fluids as a function of the local RBC concentration ϕ_l. Data is shown iodixanol ($v = 0.97$ mm/s), PVP ($v = 0.94$ mm/s), and VRF ($v = 0.59$ mm/s) at $L/D_h = 120$.

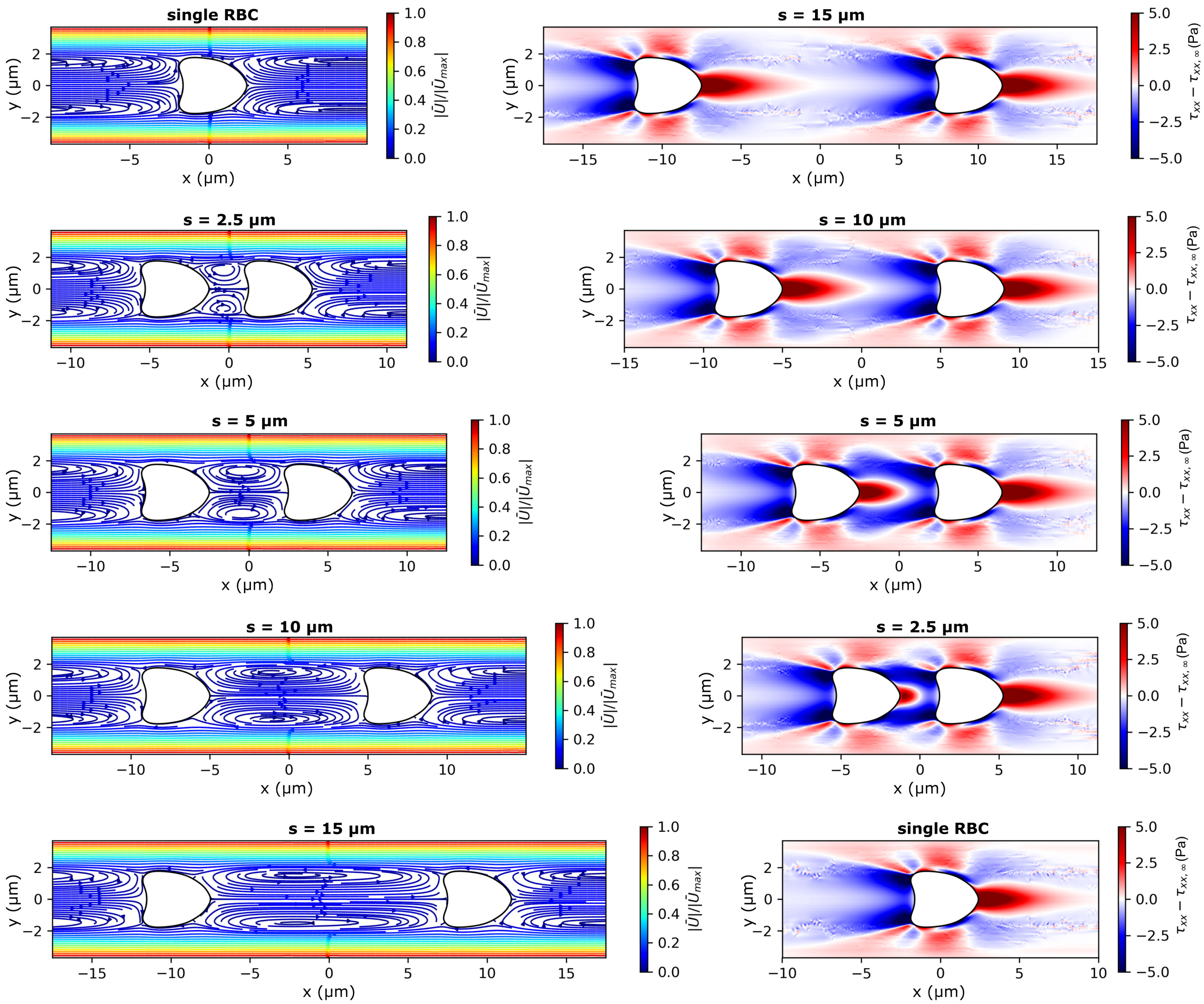

Figure S9. Numerical simulations of single cells and two croissant-shaped RBCs spaced by the surface-to-surface distance s and at $Wi = 5.0$. (Left) Streamlines of the velocity field of the system around the RBCs. (Right) Visualization of the differences in the x normal stress component of the polymeric extra-stress relative to that in an empty pipe flow ($\tau_{xx} - \tau_{xx,\infty}$).